

Experimental Study of Trailing-Edge Bluntness Noise Reduction by Porous Plates

John R. Kershner*

Lehigh University, Bethlehem, PA 18015

Justin W. Jaworski[†]

Virginia Polytechnic Institute and State University, Blacksburg, VA 24061

and

Thomas F. Geyer[‡]

o

Institute of Electrified Aero Engines, German Aerospace Center (DLR), 03046 Cottbus, Germany

https://doi.org/10.2514/1.J064045

The acoustic and aerodynamic fields of blunt porous plates are examined experimentally in an effort to mitigate trailing-edge bluntness noise. The plates are characterized by a single dimensionless porosity parameter identified in previous works that controls the influence of porosity on the sound field. Hot-wire anemometry interrogates the velocity field to connect turbulence details of specific regions to flow noise directivity and beamforming source maps. Porous plates are demonstrated to reduce the bluntness-induced noise by up to 17 dB and progressively suppress broadband low-frequency noise as the value of the porosity parameter increases. However, an increase in this parameter also increases the high-frequency noise created by the pores themselves. The same highly perforated plate characterized by a large value of the porosity parameter reduces the bluntness-induced vortex shedding that is present in the wake of the impermeable plate. Lastly, pore shape and positional alignment are shown to have a complex effect on the acoustic field. Among the porosity designs considered, plates with circular pores are most effective for low-frequency noise reductions but generate high-frequency noise. No meaningful difference is found between the acoustic spectra from plates of the same open-area fraction with pores aligned along or staggered about the flow direction.

Nomenclature

c	=	speed of sound, m/
c_l	=	chord length, m
f	=	frequency, Hz
11		havandamı larıan aha

H = boundary-layer shape factorh = boundary-layer thickness, mm

R = pore radius, mm

Re = Reynolds number based on c_l s = hole-to-hole center spacing, mm

St = Strouhal number based on plate thickness

 St_b = Strouhal number of bluntness-induced vortex shedding

Tu = intensity of the turbulent velocity fluctuations

U =free-stream velocity, m/s

 U_i = discrete measurements of the streamwise velocity at each time step, m/s

 \overline{U} = time averaged velocity at specified position, m/s

 $U_{\rm rms}$ = root-mean-square of velocity, m/s

U' = velocity fluctuation, m/s

w =plate thickness, mm

x = streamwise Cartesian coordinate, m Y = spanwise width of tunnel, m y = spanwise Cartesian coordinate, m

Presented as Paper 2023-4284 at the AIAA AVIATION 2023 Forum, San Diego, CA, June 12–16, 2023; received 7 February 2024; revision received 21 May 2024; accepted for publication 18 June 2024; published online 26 July 2024. Copyright © 2024 by John R. Kershner, Justin W. Jaworski, and Thomas F. Geyer. Published by the American Institute of Aeronautics and Astronautics, Inc., with permission. All requests for copying and permission to reprint should be submitted to CCC at www.copyright.com; employ the eISSN 1533-385X to initiate your request. See also AIAA Rights and Permissions www.aiaa.org/randp.

*Ph.D. Candidate, Department of Mechanical Engineering; jrk520@ lehigh.edu. Student Member AIAA.

[†]Associate Professor, Kevin T. Crofton Department of Aerospace and Ocean Engineering; jaworski@vt.edu. Associate Fellow AIAA.

*Senior Researcher, Formerly: Technical Acoustics Group, Brandenburg University of Technology Cottbus - Senftenberg, 03046 Cottbus, Germany; thomas.geyer@dlr.de. Member AIAA.

= vertical Cartesian coordinate, m

 α_h = open-area fraction

 γ = acoustic power exponent of U δ = dimensionless porosity parameter

 δ^* = boundary-layer displacement thickness, mm θ = boundary-layer momentum thickness, mm

 Φ = spectrum of the turbulent velocity fluctuations, m²/s

I. Introduction

N OISE measurements of live animals indicate that owls fly quieter than other birds [1,2], especially at high frequencies. This quiet flight is believed to be caused in part by the tattered fringe at the trailing edge (TE) of their wings. This edge feature has been idealized by wing porosity [3], which has been shown to reduce flow noise in a laboratory setting using guidance from theoretical analyses [2,4]. With inspiration from nature's silent flier, the owl, engineers seek to use porosity to reduce flow noise with applications to wind turbine blades, submarines, fan rotors, and even airplane wings [2,5–7]. The early theoretical and numerical work of Howe [8] on porous plate acoustics modeled a point vortex passing over a trailing edge to show that the presence of perforations could reduce trailing-edge noise significantly. Computational simulations by Khorrami and Choudhary [9] indicated that the presence of porosity on a flat plate can reduce sound by reducing the strength of the edge scattering and by modifying the hydrodynamic noise source itself.

Further experiments investigated the acoustic and aerodynamic effects of fully and partially porous airfoils in an aeroacoustic wind tunnel with a microphone array and a force balance setup to measure changes in lift and drag [10,11]. These experiments used porous SD 7003 airfoils composed of various foams, where the presence of porosity reduced aerodynamic noise by up to 10 dB for frequencies less than 10 kHz. The reductions in noise depended strongly on the flow resistivity of the porous medium, and these porous airfoils generated excess noise at frequencies above 10 kHz. Later theoretical works modeled chordwise-varying porosity inspired by the flow resistivity of owl wings in aerodynamic [12,13] and acoustic [14] contexts, where the latter study found that varying the pore distribution of perforated surfaces can lead to greater noise reductions than in

the case of uniform porosity. These studies also showed changes in directivity due to porosity and overall noise level reductions.

In addition to categorizing permeable materials by porosity, flow resistivity (which is directly connected to permeability), and tortuosity [15,16], more recent studies have characterized porous designs by their acoustic impedance. In the study by Jiang [17], porous material characteristics such as hole size and spacings were selected according to the characteristic acoustic impedance and the absorption coefficient, as measured by an impedance tube using the transfer function method of Chung and Blaser [18,19]. Their study showed that porous edge extensions, compared to a nonporous airfoil, reduce lowfrequency noise but increase noise at higher frequencies, except when paired with serrations, which are known to reduce high-frequency noise successfully [20]. The increase in noise at high frequencies has been observed and attributed in many other studies as being due to a surface roughness effect [10,11,17,21]. In addition, recent numerical simulations have shown this excess noise to be caused by an acoustic dipole arising from interactions of edge-induced flow separation with the suction-side surface of a NACA 0012 airfoil [22]. Although increases of noise by porous plates at high frequencies are welldocumented in the research literature [10,11,17,21], further experimental investigations into the mechanisms of this excess noise are warranted, and the use of porosity to reduce noise in other frequency ranges should not be discounted.

Porous designs may be tailored to reduce specific types of flow-induced noise. One of these kinds of noise is bluntness noise, which is tonal in nature and originates from vortex shedding at the TE. This kind of noise is highly dependent on edge geometry and Reynolds number and typically occurs at

$$\frac{2\pi f z_{\text{wake}}}{U} \simeq 1 \tag{1}$$

where z_{wake} is the wake scale when the ratio of the bluntness height to the boundary-layer displacement thickness is greater than 0.3 (see Table 5.3 in [23]). For the case of NACA 0012 airfoils and flat plates, bluntness vortex shedding is prevalent between chord-based Strouhal numbers of St = 0.12 and St = 0.22 [24,25].

Showkat Ali et al. [26] investigated experimentally the use of porous treatments to reduce bluntness noise occurring at $St \approx 0.2$. In their best case, they found that highly permeable materials could reduce the maximum tonal noise by 35 dB [26], but this level of noise reduction depended strongly on the permeability and volumetric porosity of porous materials. They also found that the use of porous edges helped to reduce the flow velocity and acceleration about the edge, which is thought to lead to a weakening of the vortex shedding. In addition to porous metal foams, structured porous edges have also demonstrated the ability to reduce bluntness noise in experimental studies [27]. Multiple computational studies have demonstrated the ability of porosity to reduce TE bluntness noise on flat plates. For example, in a large eddy simulation (LES) numerical campaign, Bae et al. [28] found that porous TE treatments can reduce the vortex shedding frequency by 13 dB, and Koh et al. [25] used an LES/ computation aeroacoustics method simulation that found the overall sound pressure level generated by a finite-edge flat plate can be reduced by up to 12 dB through the use of edge porosity.

Whereas these prior studies demonstrated that porosity can successfully reduce overall broadband noise and bluntness tonal noise, the question remains how porosity and its realization as a geometric design affect the acoustic power scaling on flow speed for bodies in a flow. Also, the effects of porosity in the form of pores (or perforations) on bluntness noise have yet to be investigated from a combined acoustical and hydrodynamical perspective. These technical challenges are addressed in the present work through the lens of theoretical guidance from the dimensionless porosity parameter governing the problem to discern if and when geometrical effects of porosity designs have an impact on flow noise from porous edges.

The acoustic power scaling of the radiated sound on flow speed, U^{γ} , varies between $5 \le \gamma \le 6$ for porous edges and acoustically noncompact airfoils [3,11], which is to be compared against the $\gamma = 5$ result for impermeable edges [29]. In Chen et al. [4], a time-domain

Green's function approach solves the acoustic scattering problem inspired by Kambe et al. [30] of a vortex ring passing over a semi-infinite porous plate to predict the acoustic power scaling, directivity patterns, and acoustic pressure waveforms. Their theoretical model uses a dimensionless porosity parameter, composed of physical details of the porous/perforated medium and the acoustic field,

$$\delta = \frac{2\alpha_h c}{\pi^2 f R} \tag{2}$$

which was first identified by Ffowcs Williams [31] in his analysis of infinite porous surfaces. In Eq. (2), α_h is the open-area fraction, c is the speed of sound, f is the frequency, and R is the pore radius. The porosity parameter δ , which was also referred to as μ/k in Jaworski and Peake [3] and Chen et al. [4], following the original analysis of Crighton and Leppington [32], was used by Jaworski and Peake [3] to show that the acoustic scaling of porous edge noise on flight speed becomes U^6 for large values of δ , which results in an effective decrease of noise in low-Mach-number flows. The behavior of the velocity scaling exponent γ as a function of the dimensionless porosity parameter δ is depicted in Fig. 1. The change in acoustic power scaling is accompanied by a notable change in sound directivity, from a cardioid shape at U^5 to a dipole shape at U^6 [4].

Experiments at the Applied Research Laboratory at the Pennsylvania State University were the first to experimentally investigate this parameter δ to describe how permeability affects the scattered sound field. Preliminary results from a vortex-ring setup in a quiescent fluid show favorable changes in directivity and sound power at different values of δ [33,34]. However, a companion experiment to confirm these results using a turbulent boundary layer to generate the trailing-edge noise is currently lacking.

A problem in the way of investigating the noise scaling effects of porous edges is the many noise generating mechanisms that affect the scaling such as bluntness noise. The purpose of this paper is to examine experimentally, for the first time, to the best of our knowledge, the sound field and source regions of blunt-edged porous plates, characterized by this dimensionless porosity parameter, in a fluid flow over a range of δ values. This effort is carried out using single far-field microphones and a planar microphone array to measure the acoustic field, as well as a hot-wire anemometry to measure the turbulent velocity field. Changes in sound pressure level and directivity are measured in complement to the central focus on the reduction of edge bluntness noise engendered by porous edges. The effects of pore shape and spatial distribution on the resulting acoustic and hydrodynamic fields are also analyzed.

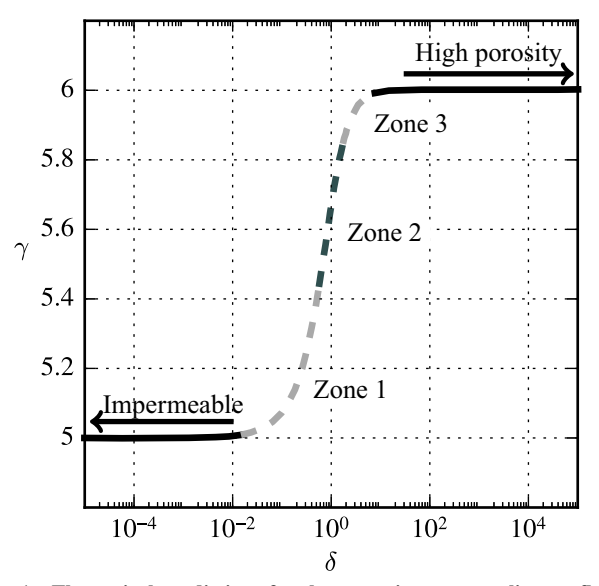


Fig. 1 Theoretical predictions for the acoustic power scaling on flow speed γ as a function of the dimensionless porosity parameter δ . Adapted with permission from Chen et al. [4]. Copyright 2022, Chen et al.

II. Methods

The experimental apparatus involves 0.17 m (chord length) \times 0.30 m (span width) $\times 0.003 \text{ m}$ (thickness) acrylic plates that are designed with various hole shapes and spacings to cover a range of values of δ . The desired parametric range of δ is determined from the theoretical analysis of Chen et al. [4]. Subsequently, three groupings of plates, with low (L), medium (M), and high (H) permeability (or porosity), are designed and presented in Table 1 and Fig. 2 to span from the effectively impermeable, to the transitional, to the highly porous behaviors of porous edge noise. In contrast to its adaption for a

Table 1 **Testplate information**

Name	Hole type	R, mm	s, mm	$\alpha_h,\%$	$\delta \times f$, Hz
L1	Circular aligned	0.9	12.5	1.6	1.24×10^{3}
L2	Circular unaligned	0.9	12.5	1.6	1.24×10^{3}
L3	Square aligned	0.9	19.5	0.86	0.664×10^{3}
L4	Square unaligned	0.9	19.5	0.86	0.664×10^{3}
M1	Circular aligned	0.9	5.0	10	7.72×10^{3}
M2	Circular unaligned	0.9	5.0	10	7.72×10^{3}
M3	Square aligned	0.9	8.0	5.1	3.94×10^{3}
M4	Square unaligned	0.9	8.0	5.1	3.94×10^{3}
H1	Circular aligned	0.9	4.0	16	12.4×10^{3}
H2	Circular unaligned	0.9	4.0	16	12.4×10^{3}
H3	Square aligned	0.9	4.9	13	10.1×10^{3}
H4	Square unaligned	0.9	4.9	13	10.1×10^3

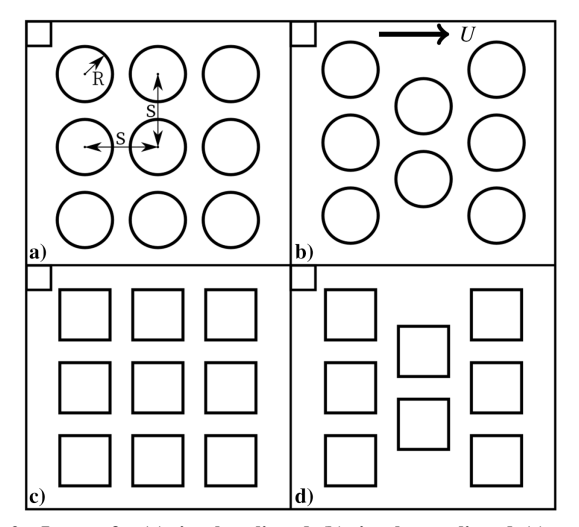
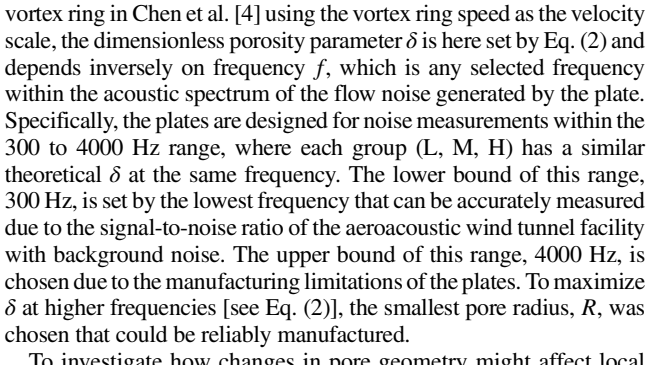


Fig. 2 Layout for (a) circular aligned, (b) circular unaligned, (c) square aligned, and (d) square unaligned holes.

zero in all studies considered here. The acoustic measurements were performed with eleven 1/4 inch free-field microphones located on an arc at one side of the test section and with a planar microphone array located at the opposite side along one wall of the test section. The data were synchronously recorded with a sampling frequency of 51.2 kHz and a duration of 40 s and stored on a RAID system. Postprocessing was performed using the open source Python package Acoular [37]. For the measurements with single microphones, the time data were transferred to the frequency domain using a fast Fourier transform (FFT) according to Welch's theorem [38], which was done on Hanning-windowed blocks with a size of 8192 samples and with an overlap of 50%, yielding a frequency



To investigate how changes in pore geometry might affect local flow and its generated noise and associated directivity, circular and square holes with both aligned and offset pore patterns (with respect to the flow direction, U) are investigated. These different hole spacings are depicted in Fig. 2. The pores are manufactured by a 75-W Universal Laser Systems model PLS6 150D laser cutter. The hydraulic radius is taken for the R term in δ in the case of square holes. The low-parameter plates, labeled starting with L (see Table 1), enable δ in Zone 1 in Fig. 1; the medium parameter plates, labeled starting with M, enable δ in Zone 2, and the high parameter plates, labeled starting with H, enable δ in Zone 3. Also, an impermeable plate is included for reference comparison. Circular and square holes are chosen to test the effect of different pore shapes, as geometrical effects (besides pore size) and their associated real flow effects are not captured by δ and are therefore unknown. Lastly, all plates were equipped with approximately 12 mm wide strips of anti-slip tape on both sides at a chordwise location of $x/c_1 = 0.10$ to force transition and thus ensure the presence of a turbulent boundary layer at the TE.

The experimental measurements were conducted in the small open jet aeroacoustic wind tunnel at the Brandenburg University of Technology in Cottbus, Germany [35], as shown in Fig. 3. The nozzle in the experiments has a rectangular exit area with dimensions of $0.23 \times$ 0.28 m and a maximum flow speed of approximately 50 m/s. Attached to the upper and lower edges of the nozzle are rectangular sideplates made of acrylic glass. Similar to the setup in [36], circular rotatable discs were set into the sideplates. The flat plates under examination were mounted at both ends to these circular discs to allow for the adjustment of the geometric angle of attack, which was

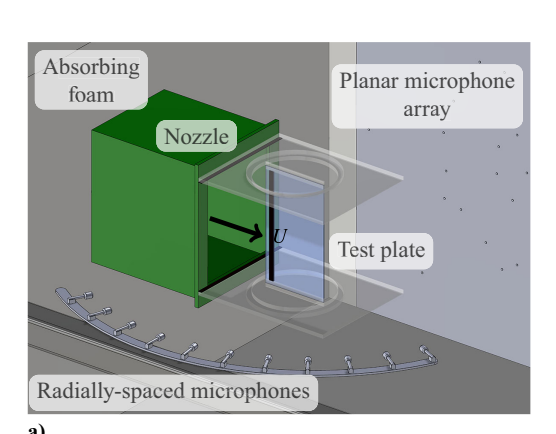




Fig. 3 (a) Labeled schematic and (b) photograph of the experimental acoustic setup inside the aeroacoustic wind tunnel.

resolution of 6.25 Hz. The results were then converted to sound pressure levels (SPLs) in decibels with a reference value of 20 μ Pa. The same FFT settings were used for the measurements with the planar microphone array, and Functional beamforming [40] was applied on the resulting cross-spectral matrix using Acoular to extract the noise source locations and magnitudes. A 6 dB level is subtracted from the beamforming result to account for the reflection at the rigid array, thus leading to results that correspond to the value a single microphone would measure at the center of the array. To test whether reflections from the planar array affected measurements from the radially spaced microphones, comparison measurements were made with the planar array uncovered and covered by an acoustically absorbent material. Acoustic spectra measured from the radially spaced microphones showed no noticeable difference between the two cases. Using the approach described in Glegg & Devenport ([41], Table 18.3), the averaging uncertainty of the autospectra based on the number of FFT blocks is 8.9%. The averaging uncertainty of the cross-spectral density magnitude (part of the cross-spectral matrix used in beamforming calculations) is 16% (approximately $\pm 1 \, dB$) at 5 kHz between the center microphone on the arc and its neighbor.

Constant temperature anemometry (CTA) measurements were performed using a DANTEC Dynamics hot-wire system and a 55P15 boundary-layer probe. The data were recorded with a sampling frequency of 25.6 kHz and a duration of 10 s. Initial measurements were taken at center span at a distance of 0.09 m from the nozzle exit to analyze the flow field it supplies without a testplate installed. This distance corresponds to the leading-edge location of the plates. The velocity profile at this location is uniform and has a

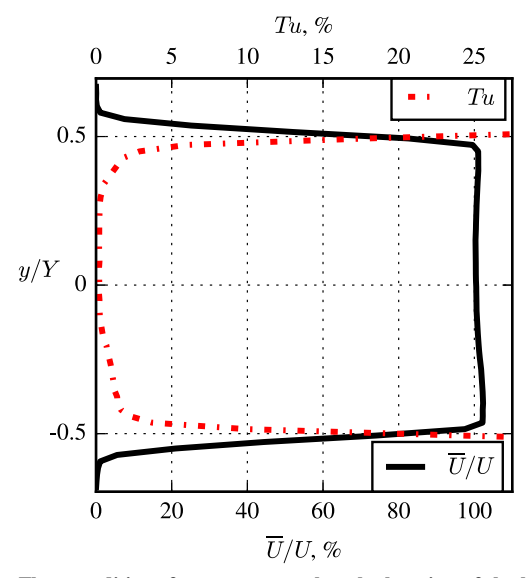
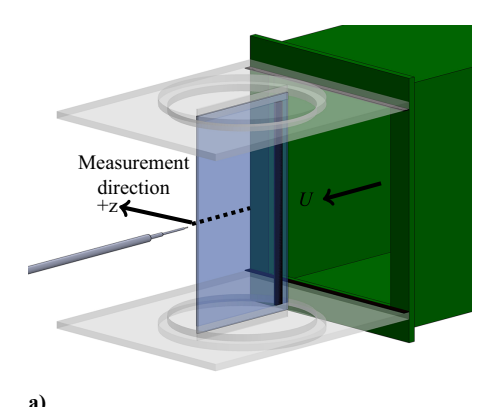


Fig. 4 Flow conditions for empty tunnel at the location of the leading edge of the plates (\overline{U}/U) and Tu for U=30 m/s).



very low turbulence intensity, Tu, of approximately 0.24% at the center point (see Fig. 4). The intensity of the turbulent velocity fluctuations is defined here as

$$Tu = \frac{U_{\rm rms}}{\overline{U}} \tag{3}$$

where the root-mean-square of the turbulent velocity fluctuations collected over N time samples is

$$U_{\rm rms} = \sqrt{\frac{1}{N} \sum_{i=1}^{N} (U_i')^2}$$
 (4)

and the turbulent velocity fluctuations are

$$U_i' = U_i - \overline{U} \tag{5}$$

Further CTA measurements were performed in the near wake and upstream boundary layer of selected plates to analyze the flow field and how it is affected by the presence of porosity. These temporal data of the turbulent velocity fluctuations were transferred to the frequency domain using the same functions described previously for the acoustic signals to obtain the spectra of the turbulent velocity fluctuations, Φ , with a frequency resolution of 3.125 Hz.

To understand more about the porous plates' effects on the boundary layer, the boundary-layer thickness, displacement thickness, momentum thickness, and shape factor are calculated from the CTA data. The boundary-layer thickness, h, from experimental measurements is taken as the height where the mean velocity reaches 99% of the freestream velocity. The boundary-layer displacement thickness, δ^* , and the momentum thickness, θ , are calculated in the standard manner [42],

$$\delta^* = \int_{z=0}^{\infty} \left(1 - \frac{\overline{U}(z)}{U} \right) dz \tag{6}$$

$$\theta = \int_{z=0}^{\infty} \left(1 - \frac{\overline{U}(z)}{U} \right) \cdot \left(\frac{\overline{U}(z)}{U} \right) dz \tag{7}$$

The shape factor,

$$H = \frac{\delta^*}{\theta} \tag{8}$$

follows as the ratio of the displacement thickness and momentum thickness. The measurement setup is detailed in Fig. 5a, and Fig. 5b illustrates the streamwise x and spanwise y locations of the measurements.

The CTA measurements were taken in two regions of the plate: 1 mm behind the TE in the near-wake region and 5 mm upstream from

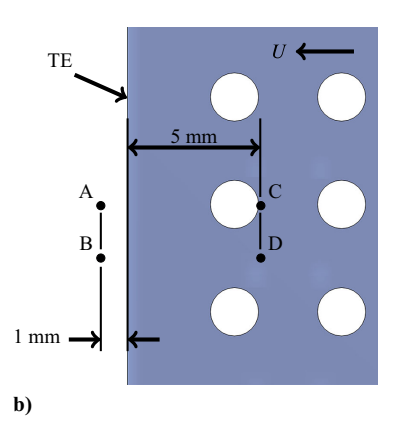


Fig. 5 (a) CTA setup schematic and (b) closeup on porous TE with labeled spanwise and chordwise positions for the near-wake (A and B) and upstream (C and D) measurements.

the TE. The measurement locations for the near wake are labeled as points A and B, and the upstream measurement locations are labeled as points C and D in Fig. 5b. The spanwise location of points A and C is aligned with the center of a pore, and the spanwise locations of points B and D are aligned with the gap between two pores. The nearwake measurements sweep from one side of the plate to the other in the vertical direction, and the upstream measurements begin at a distance of 2.5 mm from the plate surface to ensure that the probe did not accidentally come in contact with the testplate. Using the approach of Glegg & Devenport ([41], Table 18.1), the averaging uncertainty of the mean velocity profiles, measured in the free stream of the tunnel at 30 m/s is 0.0038%, and the velocity root-mean-square error based on the total number of samples is 0.28%. The averaging uncertainty of the spectrum of the turbulent velocity fluctuations based on the number of FFT blocks is 26% (approximately $\pm 1 \, dB$ at -30 dB). All uncertainty values are given at a 95% confidence level, and the errors are assumed to random and distributed normally.

III. Results

A. Sound Pressure Level Spectra and Soundmaps

Results are shown and discussed for the impermeable reference plate and for the perforated plates described in Table 1 and shown in Fig. 2. The flow speeds range from 9 m/s < U < 40 m/s, which yield an estimated chord-based Reynolds number range of $1.03 \times 10^5 < Re < 4.48 \times 10^5$. Strouhal number-domain spectra from the radially spaced microphone at 90° to the flow (see Fig. 3) for the impermeable plate at all flow speeds are shown in Fig. 6. The Strouhal number, St, is calculated using

$$St = \frac{fw}{U} \tag{9}$$

where w is the plate thickness.

In general, these sound pressure level (SPL) spectra increase in magnitude with increasing velocity (Reynolds number) and have sharp tonal peaks at the bluntness-induced, vortex-shedding Strouhal number. Looking to Fig. 6, the place where the peaks occur is referred to as St_b , or the Strouhal number of bluntness vortex shedding, and these values span $0.18 < St_h < 0.25$. The variation of St_h with Re is shown in Fig. 7 With the exception of the lowest Re case, the range of St_b is similar to findings from [17,26] and within the range of 0.12 < St < 0.22 found in Vathylakis et al. [24], which is denoted by the dashed horizontal lines. In addition to this comparison of St_b with those found in other experimental works, the bluntness noise peak was also predicted in the same third-octave band using an analytical model [43]. A small outlier in the data is the St_b peak in the spectra recorded at $Re = 2.05 \times 10^5$, where the peak amplitude is slightly lower than expected as it is nearly the same height as that recorded at $Re = 1.45 \times 10^5$. This was seen over multiple test days, and it is thought to be the result of an unknown physical mechanism of the tunnel.

To examine how the porous plates affect the acoustic spectra, including the bluntness-induced vortex shedding peak, Fig. 8

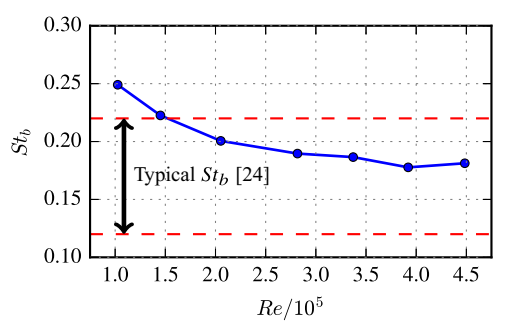


Fig. 7 Dependence of bluntness-induced vortex shedding Strouhal number, St_b , on Re for the nonporous plate.

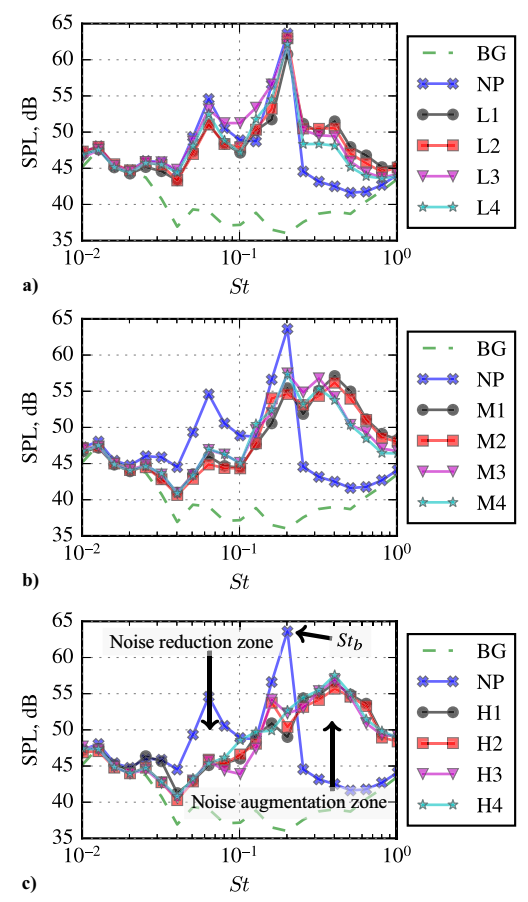


Fig. 8 Dependence of SPL on St at $Re = 3.37 \times 10^5$ for (a) low-, (b) medium-, and (c) high-porosity plates.

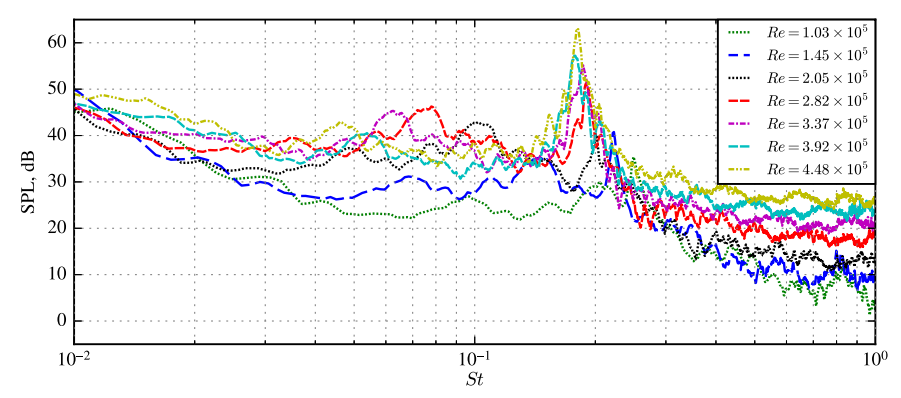


Fig. 6 Dependence of SPL on the edge-thickness based Strouhal number, St, for the nonporous plate at all tested Reynolds numbers.

shows sound pressure spectra in third-octave bands recorded by the 90° microphone as a function of Strouhal number at a selected Reynolds number, $Re = 3.37 \times 10^{5}$, for the low-, medium-, and high-porosity groupings of plates compared to the background noise of the empty tunnel and nonporous plate labeled BG and NP, respectively.

With increasing α_h and therefore δ come increasing reductions of the bluntness noise peak. Within these spectra are three main areas of interest: $0.02 < St < St_b$ where the porous plates reduce broadband noise, St_b where the porous plates greatly reduce the bluntnessinduced vortex shedding tonal noise, and $St > St_b$ where the porous plates create excess noise. Within the low Strouhal number range of $0.02 < St < St_b$, the porous plates can reduce third-octave band SPLs up to 10 dB (see Fig. 8c). In addition, SPL of the third-octave band that contains the St_b can be reduced by up to 16 dB. These reductions come at a cost, as an increase in porosity leads to an increase in excess noise at $St > St_h$. High-frequency excess noise has been noted in many other experimental investigations of porous edges [10,11,27], as well as in simulations of porous [22] and dimpled edges [44]. The ability of the porous plates to attenuate low-frequency and bluntness noise diminishes as the porosity parameter decreases. The low-porosity plates in Fig. 8a have only a modest effect on the low-frequency noise and reduce the bluntness noise peak by approximately 2 dB. The results for the medium-porosity plates in Fig. 8b lie between those of the low- and high-porosity plates. The trend whereby porosity reduces lowfrequency noise below the St_h but increases high-frequency noise beyond the St_b is seen at all flow speeds.

Beamforming results, in tandem with the raw spectra, help to make sense of the acoustic effects of the perforated plates. Figure 9 show soundmaps calculated using the Functional deconvolution beamforming algorithm at $Re = 3.37 \times 10^5$, the same Re as is presented in Fig. 8, of the nonporous and highly porous plate H1 at Strouhal numbers within the three aforementioned areas of interest: low Strouhal number broadband noise reduction, bluntness-induced vortex shedding tonal noise reduction, and excess high Strouhal number noise. Within Fig. 9, the testplate

(blue line), sideplates (gray line), and nozzle (green line) are labeled accordingly, and the flow direction is left to right.

The high porosity plates in Fig. 8c are successful at reducing the low-frequency noise below the frequency of the tonal noise peak and can greatly reduce the magnitude of the peak (see soundmaps in Figs. 9a and 9b). Figure 9a illustrates that the location of the bluntness noise from the nonporous plate is centered on and along the TE. Again, these reductions come at the cost of an increase in high-frequency noise at frequencies greater than the bluntness noise peak (see soundmaps in Figs. 9c and 9d), where excess high-frequency noise is generated on the porous plate across the entire perforated area. Soundmaps at frequencies below the bluntness shedding peak are not shown, as most common beamforming methods are known to perform poorly at low frequencies due to limitations of the setup [45].

The different pore geometries have a noticeable effect on the noise spectra, as well. In general, the plates with circular perforations are more successful at reducing the bluntness noise peak. For the highporosity set, the plates with square holes (H3, H4) reduce lowerfrequency noise slightly better than those with the circular pores (H1, H2), but this trend is reversed at Strouhal numbers greater than 0.2 (see Fig. 8c). The opposite is true for the medium- and lowporosity plates, where the circular pores produce the greatest lowfrequency noise reductions but also produce more high-frequency noise (see Figs. 8a and 8b). It was hypothesized in this study that offsetting the holes in the flow direction (plates L2, M2, and H2) may lead to a reduction in roughness noise due to the increase in streamwise spacing and therefore larger characteristic separation length between holes. However, no meaningful differences in the shape of the acoustic spectra are found between plates of aligned and offset holes with the same frequency-based δ .

Figures 10 and 11 summarize how the bluntness vortex shedding peak changes with Strouhal number for the porous plates and how the different porous plates reduce the SPL of this tonal peak. In general, Fig. 10 shows the bluntness peak reduces in Strouhal number with an increase in Reynolds number for the porous plates, which follows the trend of nonporous plates. Although the L1 plate had the highest St_h

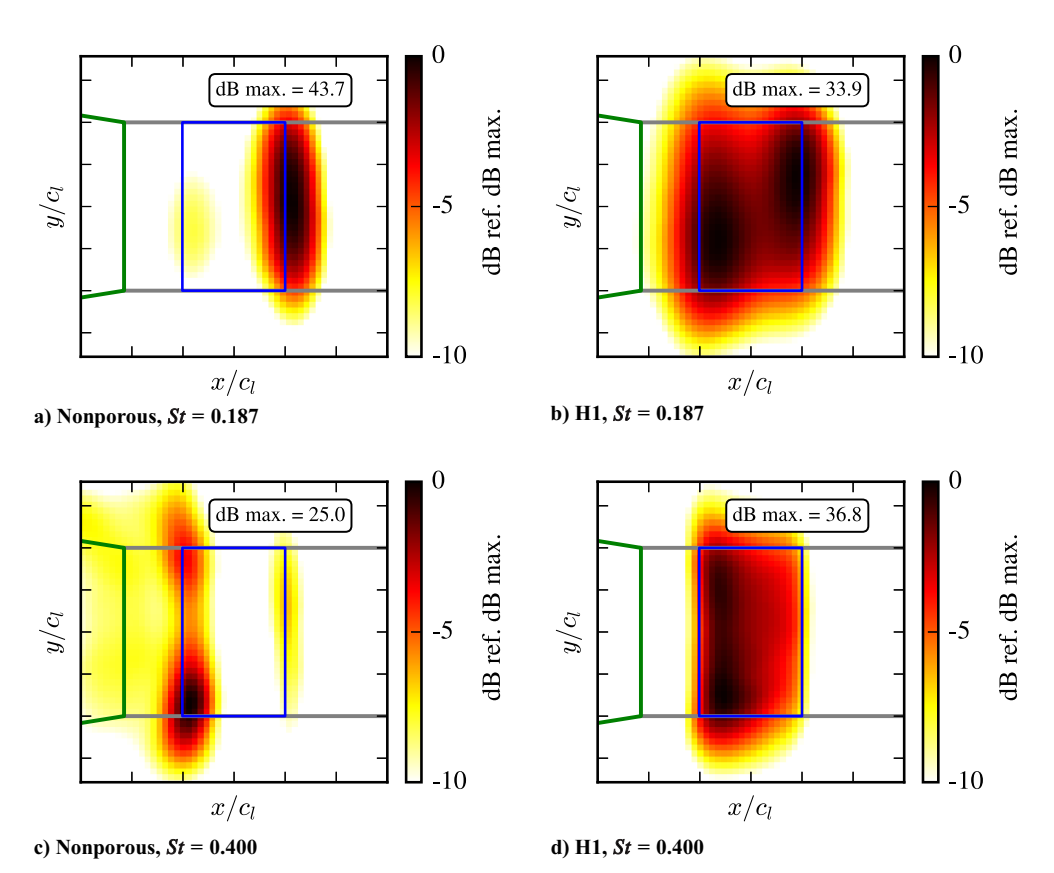


Fig. 9 Beamforming results for nonporous (left) and H1 porous (right) testplates at different third-octave bands centered on multiple Strouhal numbers at $Re = 3.37 \times 10^5$.

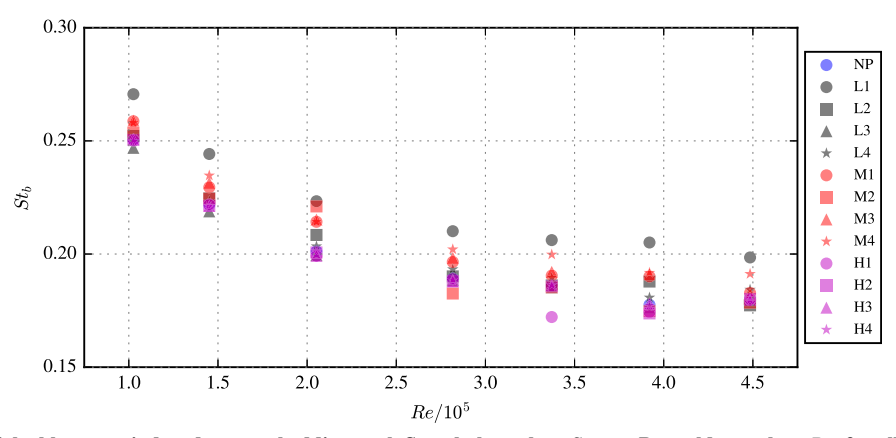


Fig. 10 Dependence of the bluntness-induced vortex shedding peak Strouhal number, St, on Reynolds number, Re, for all plates and flow speeds.

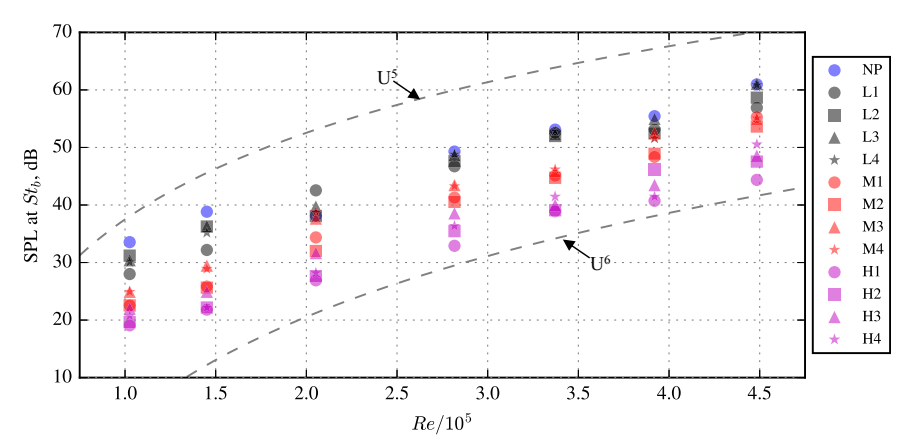


Fig. 11 SPL at St_b as a function of Re for all plates and flow speeds.

at all velocities and the medium plates typically resulted in a higher St_b than that of the nonporous plates, it is challenging to find a trend that describes the relationship between pore shape and bluntness peak within the same porosity group. One thing to note is that in Fig. 10, the highly porous plates have an St_b close to that of the nonporous plate as they all virtually eliminate the bluntness peak from the spectra, thus making it challenging to discern. The significant reduction in bluntness noise at high Reynolds numbers has a positive outlook for the applications of this work, where modern applications of flow noise reduction technologies, for example, wind turbines, operate in higher Reynolds numbers [46].

Figure 11 displays the amplitude of the bluntness-induced vortexshedding peak generated by each plate across all tested Reynolds numbers. In general, an increase in the porosity parameter is accompanied by a reduction of the bluntness noise; the maximum decrease in tonal noise occurs for plate H1 at $Re = 2.82 \times 10^5$ with an attenuation of 17 dB. Notable deviations in this overall trend occur at $Re = 2.02 \times 10^5$, where some of the low-porosity plates increase the noise at the bluntness peak. This effect may be explained by the relatively low initial amplitude at the St_b peak of the nonporous plate at this Reynolds number, as shown in Fig. 6. For qualitative comparison, Fig. 11 includes the U^5 and U^6 trends, in the form of dashed lines, that are expected from the scaling of sound sources scattered by an impermeable [29] or highly porous edge [3,4], respectively. The bluntness noise levels do not trend with these theoretical scattering predictions at lower Reynolds numbers. However, these data begin to approach the acoustic scattering trends at higher values of Reynolds number. It is important to note that the creation of tonal noise due to vortex shedding is a different physical mechanism than the trailingedge scattering mechanism for which these scaling relationships were determined. These observations suggest a focused study that is beyond the scope of the present work to reconcile the possible interaction of the vortex-shedding and acoustics scattering noise mechanisms as a function of the Reynolds number.

B. Changes to Overall Sound Pressure Levels and Directivity

In addition to the effect of the different porosities on the far-field noise spectra, their effect on the total noise is also analyzed. This analysis is carried out by evaluating the changes to the overall sound pressure level (OSPL),

$$OSPL = 10\log_{10}\left(\sum_{i} 10^{SPL_i/10 \, dB}\right) dB \tag{10}$$

where SPL_i is the sound pressure level at each frequency band from 300 to 10,000 Hz calculated using the process described in Sec. II. Figure 12 shows the OSPL vs Re for each grouping of the porous plates compared to the background noise (BG) of the tunnel and the nonporous plate (NP), as measured by the center microphone. The maximum reduction in OSPL due to porosity is approximately 3 dB for plates H1 and H2. This relatively small reduction in OSPL is due to the porous plate creating excess roughness noise at high frequencies. Whereas plates H1 and H2 (with circular pores) are the most successful of the high-porosity grouping, the overall performance of the plates in the medium- and low-porosity groupings varies greatly with hole geometry and Re, as M4 performed slightly better than M2 at high velocities. However, this ordering is the opposite at lower velocities.

This trend of slight reductions in noise can be further visualized by polar plots of OSPL calculated at all 11 radially spaced microphone locations. Figure 13 shows the OSPL for the reference plate and porous plates L2, M2, and H2 at different Re. The porous plates M2 and H2 are able to reduce the OSPL at nearly all measured angles and flow speeds. However, the ability of plate L2 to decrease OSPLs depends on the flow speed and microphone number. At $Re = 1.03 \times 10^5$, the measured OSPLs from each plate were nearly identical. At the remaining velocities, the L2 plate was nearly the same level as the impermeable, and the levels of the M2 and H2 plates were nearly identical

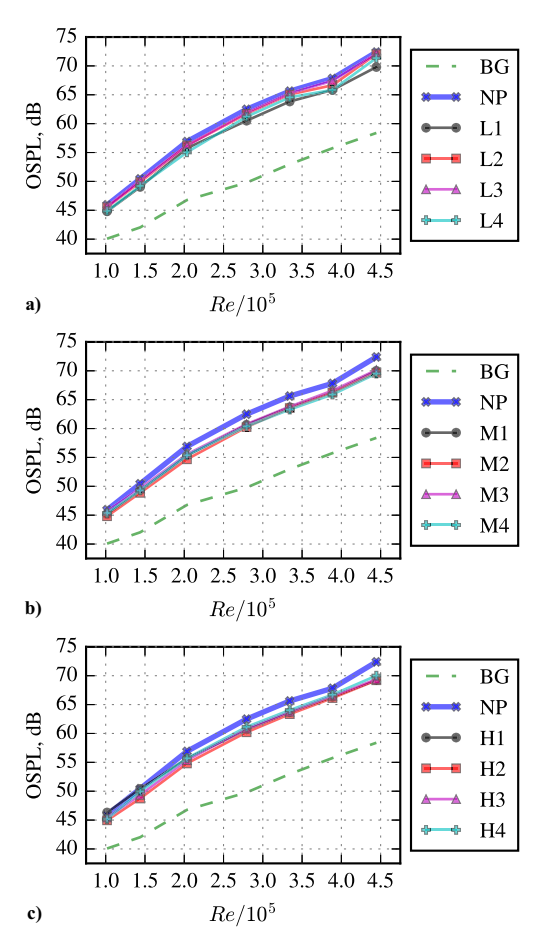


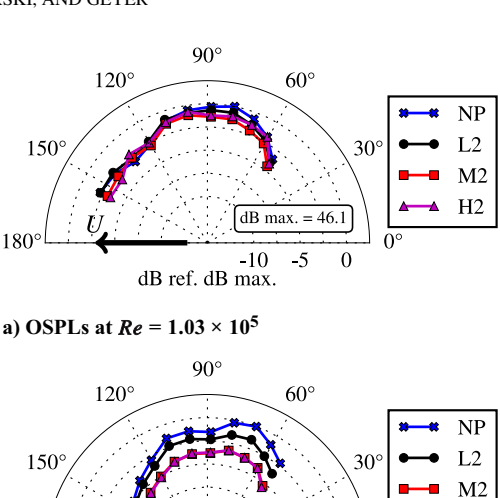
Fig. 12 Dependence of OSPL on Re for (a) low-, (b) medium-, and (c) high-porosity plates.

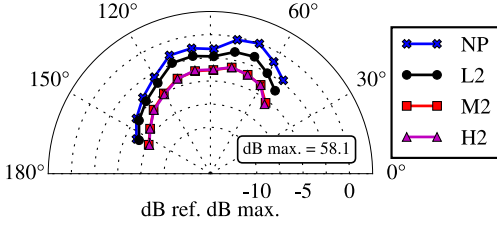
and just slightly lower than those of the impermeable. On average, at $Re = 4.48 \times 10^5$, the H1 and H2 plates achieved an OSPL reduction of up to 3 dB. This demonstrates how the low frequency, $St < St_b$, and bluntness noise reductions by increased porosity are counteracted by the increase in roughness noise at $St > St_b$. Interestingly, with an increase in Reynolds number and porosity, the directivity approaches a dipole shape. To further investigate the changes in directivity of specific Strouhal numbers, Fig. 14 is shown.

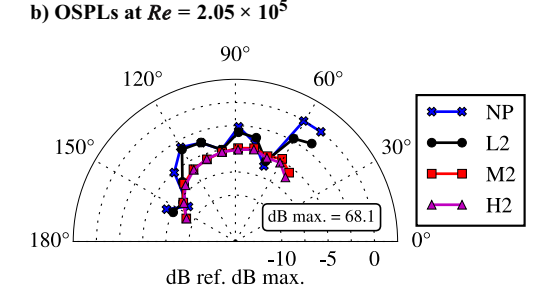
Figure 14 displays the directivity of sound generated by the nonporous plate and select porous plates at three key Strouhal numbers at $Re = 3.37 \times 10^5$. Figure 14a displays the SPL at each of the arc microphones for St = 0.075, at Strouhal number where porous plates create broadband noise reduction. In general, an increase in porosity leads to an increase in noise reduction. Figure 14b displays the directivity at the bluntness noise peak, St = 0.187, and clearly illustrates how increasing porosity, from plates L2, to M2 and H2, leads to an increased reduction of the bluntness noise peak. At St = 0.187, there is a slight trend toward a dipole directivity shaped when compared to the results at St = 0.075. Lastly, Fig. 14c displays the directivity of sound at a relatively high Strouhal number, St = 0.400. With an increase in porosity, an increase in noise is seen at each of the microphones. Within the range of $St > St_b$, the high-frequency excess noise dominates the spectra of the porous plates.

C. Flow-Field Analysis

To further investigate the suspected source of the bluntness-vortex shedding and the associated tonal peaks, hot-wire anemometry tests were conducted at a flow speed of U=30~m/s ($Re=3.37\times10^5$) in the near wake and upstream from the TE of the nonporous plate and a selected porous plate, H1. The H1 plate was chosen for its ability to best reduce the tonal peak noise among the plate specimens considered. The CTA probe traversed away from the edge in the vertical direction, z. The resulting velocity profiles from the near-







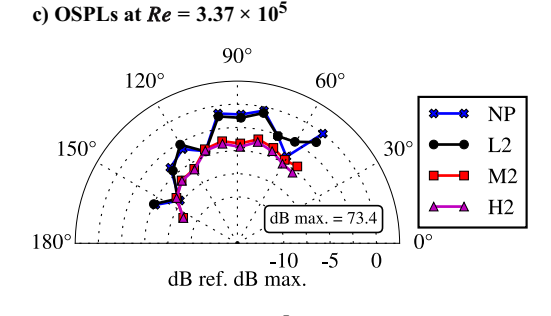


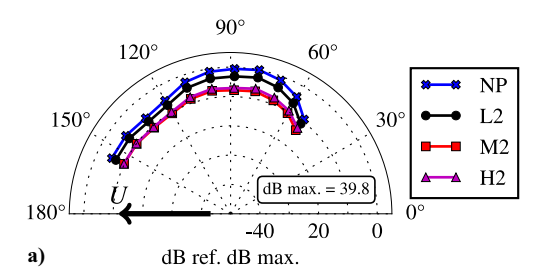
Fig. 13 OSPLs measured at each radially spaced microphone (see Fig. 3) at different Reynolds numbers and porosity treatments.

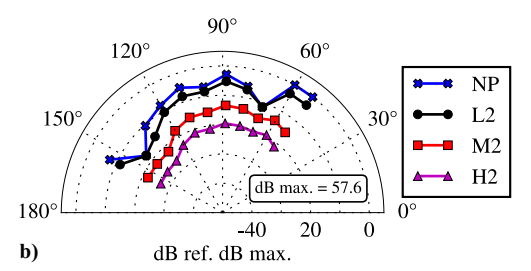
d) OSPLs at $Re = 4.48 \times 10^5$

wake and upstream measurements of the nonporous and porous plates are shown in Fig. 15. The theoretical boundary-layer height is also shown in Fig. 15 as a yellow star. To aid in viewing, every other measurement location is plotted and represented by a marker, and all of the points are connected with a spline fit.

Figure 15a shows the velocity profiles measured in the near wake of the nonporous and H1 porous plate, where the vertical axis, the distance from the testplate, is normalized by the nonporous boundary-layer height, $h_{NP}=6.4\,\mathrm{mm}$. The h measured behind a pore (labeled H1, hole) on the porous plate, measured at point A in Fig. 5b, is 4.6 mm, and the h measured along the plate between pores (labeled H1, gap) at point B is 4.8 mm. The boundary-layer thickness from the porous cases is smaller than that of the nonporous case. In addition to estimating the boundary-layer height, other relevant boundary-layer parameters are calculated.

Table 2 details this boundary-layer thickness h along with the displacement thickness, δ^* , momentum thickness, θ , and shape factor, H, that are calculated from near-wake measurements of nonporous and porous H1 plates. In addition to the smaller boundary-layer height, the porous plates also have smaller displacement and momentum thicknesses. The reduction in boundary-layer height and displacement





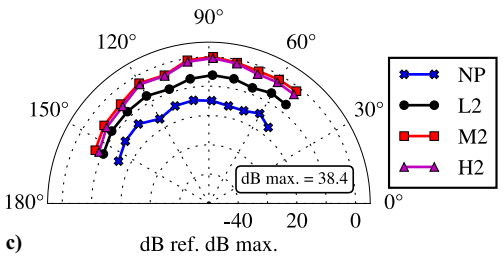


Fig. 14 Directivity of sound generated by nonporous plates and select porous plates at (a) St = 0.075, (b) St = 0.187, and (c) St = 0.400 at $Re = 3.37 \times 10^5$.

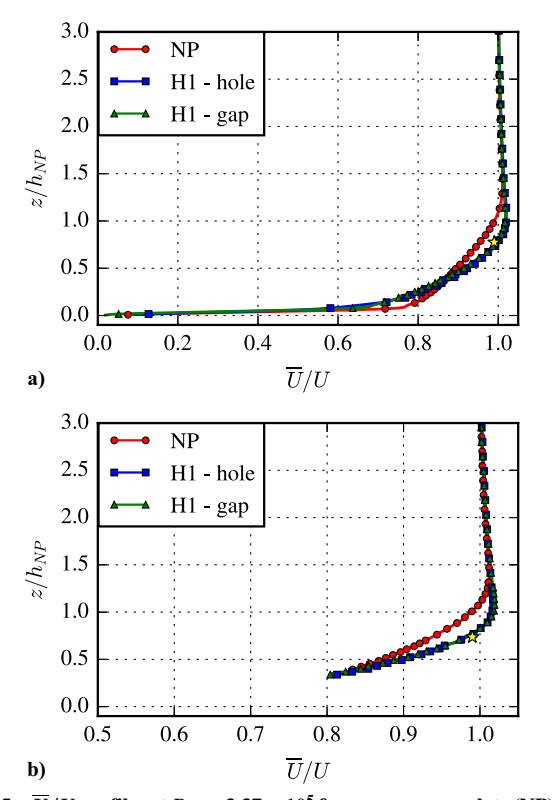


Fig. 15 \overline{U}/U profiles at $Re=3.37\times 10^5$ from nonporous plate (NP) and H1 plate measured in (a) near-wake and (b) upstream of the TE.

Table 2 Near-wake boundary-layer measurement data for nonporous and porous plate H1

Plate	Measurement location	h, mm	δ^* , mm	θ , mm	Н
Nonporous	Near wake	6.4	0.79	0.54	1.5
H1, hole	Near wake, point A	4.6	0.69	0.41	1.7
H1, gap	Near wake, point B	4.8	0.73	0.43	1.7

thickness could help to explain reductions in broadband and tonal noise of the plates, as aeroacoustic theory says that the mean-squared sound pressure generated by trailing-edge noise is proportional to the turbulence scales [29], and turbulence scales are taken to be proportional to the boundary-layer height. In addition, the higher shape factor measured for the porous plates indicates a condition similar to the effect of a stronger adverse pressure gradient, which therefore could lead to earlier separation.

Velocity profiles measured at 5 mm upstream from the TE and normalized by the nonporous boundary-layer height h_{NP} , at this location, are shown in Fig. 15b. The probe began its measurements at a position 2.5 mm from the plate surface and moves away in the vertical direction. The boundary-layer height for porous plate measured at a hole (point C in Fig. 5b) is 4.9 mm and is 5.0 mm measured at a gap (point D). Finally, the boundary-layer height for the nonporous case is 6.5 mm. Compared to measurements in the near wake, the boundary-layer height is slightly larger when measured upstream. This increase in boundary-layer height at the location of the pores could support the hypothesis that the pores create additional turbulence. The turbulence intensity profiles are subsequently analyzed to investigate this hypothesis further.

Figure 16 displays the turbulence intensity from the same set of measurements as shown in the velocity profile figures for the non-porous (NP) and H1 plate. For both test locations, the near wake and upstream of the TE, the turbulence intensity measured close to the porous plate is greater than that of the nonporous plate. In Fig. 16a, the turbulence intensity measured in the near wake behind a hole in the streamwise direction was the greatest. This trend is also seen in the turbulence intensity profiles measured upstream of the TE in Fig 16b. The higher turbulence intensity near the porous plate surface

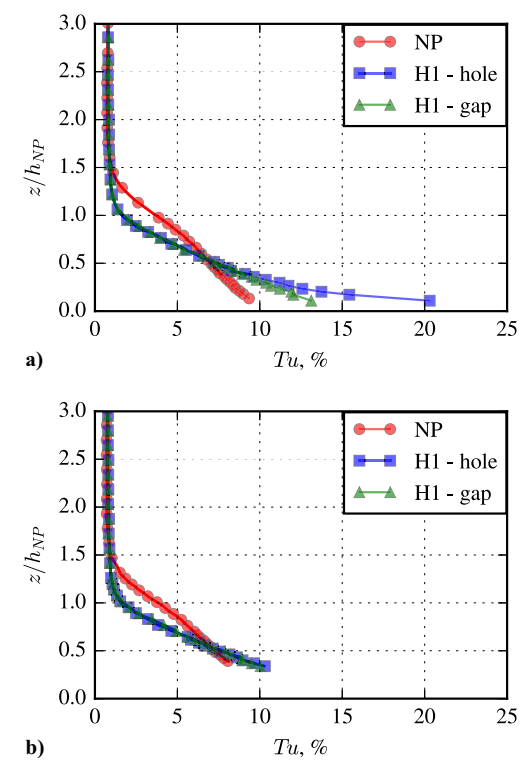


Fig. 16 Tu profiles at $Re = 3.37 \times 10^5$ from nonporous plate (NP) and H1 plate, measured in (a) near-wake and (b) upstream of the TE.

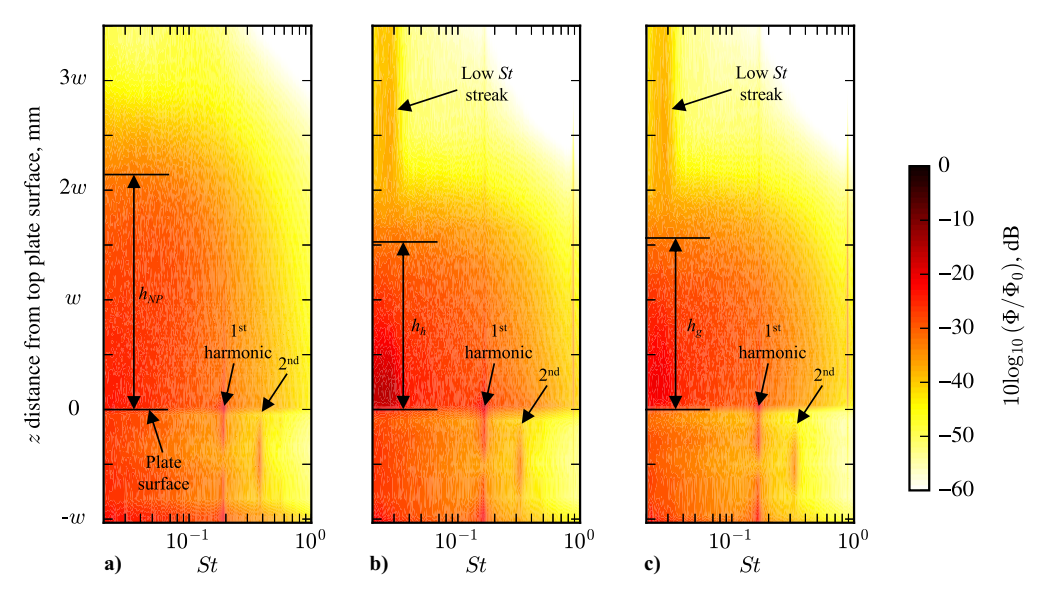


Fig. 17 Spectra of near-wake turbulent velocity fluctuations, for (a) nonporous plate and (b) porous plate H1 behind hole and (c) behind gap at $Re = 3.37 \times 10^5$.

could help to explain how pores may create excess turbulence, which could in turn explain the excess noise at high Strouhal numbers. Beyond a height of approximately $z/h_{NP}\approx 0.6$ in both the near-wake and upstream measurement locations, the turbulence intensity of the nonporous becomes greater than that of the porous plate. This result is likely due to the fact that the porous plate BL is smaller, and, at this distance, the probe is starting to move out of the BL and into the freestream. Further information from the CTA measurements is gained by analyzing the spectra of the turbulent velocity fluctuations in the following figures.

Figure 17 shows contour maps of the spectra of the turbulent velocity fluctuations from the near-wake measurements shown in Fig. 15a. These contour maps show $10 \log_{10}(\Phi/\Phi_0)$, where Φ is the spectrum of the turbulent velocity fluctuations and $\Phi_0 = 1 \text{m}^2 \text{s}^{-1}$. These data are presented in terms of the Strouhal number and measurement position. Within each subfigure, the boundary-layer thickness is shown and labeled h_{NP} for the nonporous case and h_h and h_g for the porous hole and gap measurements, recorded at points A and B in Fig 5b, respectively. Figure 17a shows the results from the nonporous plate, where a significant peak in the turbulence is seen at St = 0.19 that is consistent with that of the acoustic peak due to

bluntness. This peak is pronounced and dissipates at a distance of approximately 3w away from the edge. A resonance of this peak is also seen at St=0.38. Results from the porous plate H1 are shown from measurements taken directly behind a perforation and directly behind a gap between two perforations in Figs. 17b and 17c, respectively. These measured spectra show a notable lack of a tonal peak at St=0.19 when compared to the nonporous plate. However, strong peaks reappear instead at St=0.17 and a harmonic at St=0.34 in both hole and gap measurements about the porous plate. Another interesting feature of the contour plots is a decrease in turbulence intensity at the middle of the plate, z=-w/2, which could be due to little or no flow circulation existing in this region directly downstream of the center of the TE.

The downward shift of tonal peaks from St = 0.19 (nonporous) to St = 0.17 (porous) is seen in the turbulence intensity measured in the wake of the plates and is observed in the acoustic spectra from the plates. However, the acoustic tonal peak is much less pronounced as it is removed by the presence of porosity. The measured downward shift could be due to the thinner boundary layer of the porous plate (see Fig. 15) creating and therefore the length scale of the largest turbulent structures being smaller, as well. These results also suggest

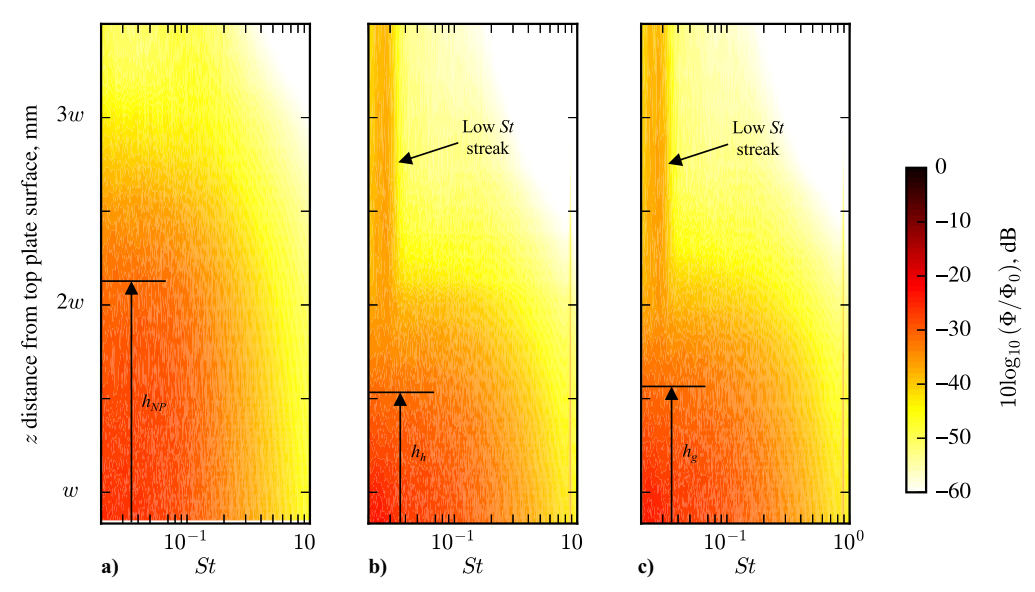


Fig. 18 Spectra of upstream turbulent velocity fluctuations, for (a) nonporous plate and (b) porous plate H1 behind hole and (c) behind gap at $Re = 3.37 \times 10^5$.

that the tonal noise might not always scale with a geometric dimension of the plate, but instead the wake vortex shedding could scale on a fluid-dynamic dimension that is yet to be identified. This idea is similar to the findings of a previous experimental work on cylinders in a cross-flow [47], where the wake width was found to be an effective scaling factor. Additional measurements or simulations are necessary to further substantiate this claim.

Figure 18 displays contour maps of the turbulent velocity spectra measured upstream from the TE. These measurements began 2.5 mm from the plate surface in the z direction, and, for that reason, the vertical axis is changed from that in Fig. 17. The contour plots from the upstream CTA measurements are very similar to those from the near-wake measurements. The nonporous plate has an overall larger region of increased turbulence, attributed to the larger boundary-layer thickness. However, like in the near-wake measurements, the porous plates have a region of higher turbulence seen in the range 0.03 < St < 0.04 which is recorded at all z locations. This corresponds to a frequency of 300 Hz < f < 400 Hz. Interestingly, the acoustic spectra of the porous plates do not contain increases at these frequencies. This excess turbulence could either be not scattered at the trailing edge, or it might not relate to far-field noise in the directivity we are considering. Additional work is necessary to identify the source of this low Strouhal number turbulence present in both the near-wake and upstream velocity field of the porous plates. Lastly, the tonal peak due to bluntness vortex shedding at St_b seen between w < z < 2 w in the near-wake measurements is not present in the upstream measurements. The absence of the St_b in the upstream velocity spectra helps to confirm that the St_b peak in both the acoustic spectra and nearwake velocity spectra is indeed due to vortex shedding occurring in

IV. Conclusions

An experimental program was carried out to evaluate trailing-edge bluntness noise and its overall reduction using perforated plates. The plates were designed with pore geometries and spacings to fit three groups of a dimensionless porosity parameter δ , and results of the farfield sound pressure level spectra and the overall sound pressure level for various Reynolds numbers were presented. Bluntness vortex shedding noise is present between $0.17 < St_b < 0.25$, and the highest porosity plates can reduce this noise by up to 17 dB, effectively removing the peak from the acoustic spectra. The relationship between hole shape and arrangement with the noise spectra is complex, where the plates with circular holes are more effective in general at reducing the bluntness noise peak. However, the plates with holes along the flow direction attenuate low-frequency noise slightly better than plates with staggered hole placement at most flow speeds. An increase in open-area fraction α_h (and consequently, the dimensionless porosity parameter δ), regardless of shape or pore alignment with the flow, leads to an increase in high-frequency noise due to the many surface elements (i.e., holes or pores) acting as noise sources. Directivity plots of the sound pressure level at a low Strouhal number where broadband noise is reduced by porosity, the bluntness noise peak Strouhal number, and a high Strouhal number where excess noise is created by porosity show a trend toward the anticipated dipolar shape with increasing porosity parameter.

Complementary analysis of the flow field using hot-wire anemometry shows that porous plates have smaller boundary-layer thickness, displacement thickness, and momentum thickness than a nonporous plate in the same flow condition, similar to previous experimental investigations of a grazing flow over a permeable wall [48]. There is also a coupling between the wake and the acoustics, where the turbulence and acoustic spectra are nearly aligned at the bluntness peak for the nonporous plate. However, results from the porous plate show a misalignment where the peaks in the turbulence spectra are shifted toward lower Strouhal numbers, which is seen in the acoustic spectra but is much less pronounced. Also, the pressure-release effect of the perforations on the plate leads to a decreased turbulence intensity when moving farther away from the plate and to a shift of the tonal vortex shedding peak.

These results motivate future investigations into the mechanisms leading to the downward shift of the bluntness-induced vortex shedding peak in the turbulence spectra. As partially porous airfoils tend to reduce the excess high-frequency noise caused by perforations, future work could also investigate the viability of partially porous airfoils to reduce bluntness noise without the added downside of excess high-frequency noise.

Funding Sources

The authors acknowledge the support of the German-American Fulbright Commission, The Germanistic Society of America, and NSF CAREER award 1846852.

Acknowledgments

The authors thank Stefan Rohark at the Brandenburg University of Technology and the Lehigh Design Labs for their assistance with manufacturing the experimental setup and the porous plates. Dr. Michael Krane at ARL Penn State is also gratefully acknowledged for insightful conversations and mentoring.

References

- [1] Sarradj, E., Fritzsche, C., and Geyer, T. F., "Silent Owl Flight: Bird Flyover Noise Measurements," *AIAA Journal*, Vol. 49, No. 4, 2011, pp. 769–779. https://doi.org/10.2514/1.J050703
- [2] Jaworski, J. W., and Peake, N., "Aeroacoustics of Silent Owl Flight," Annual Review of Fluid Mechanics, Vol. 52, No. 1, 2020, pp. 395–420. https://doi.org/10.1146/annurev-fluid-010518-040436
- [3] Jaworski, J. W., and Peake, N., "Aerodynamic Noise from a Poroelastic Edge with Implications for the Silent Flight of Owls," *Journal of Fluid Mechanics*, Vol. 723, May 2013, pp. 456–479. https://doi.org/10.1017/jfm.2013.139
- [4] Chen, H., Yoas, Z. W., Jaworski, J. W., and Krane, M. H., "Acoustic Emission of a Vortex Ring Near a Porous Edge. Part 1: Theory," *Journal* of Fluid Mechanics, Vol. 941, June 2022, Paper A28. https://doi.org/10.1017/jfm.2022.313
- [5] Blake, W. K., Mechanics of Flow-Induced Sound and Vibration, Volume 1: General Concepts and Elementary Sources, Academic Press, New York, 2017.
- [6] Schepers, J., Curvers, A., Oerlemans, S., Braun, K., Lutz, T., Herrig, A., Wuerz, W., Mantesanz, A., Garcillan, L., Fischer, M., et al., "SIROCCO: Silent Rotors by Acoustic Optimisation," 2nd International Meeting on Wind Turbine Noise, Inst. of Noise Control Engineering/Europe (ICNE/ Europe), Paper ECN-M-07-064, 2007.
- [7] Leylekian, L., Lebrun, M., and Lempereur, P., "An Overview of Aircraft Noise Reduction Technologies," *Aerospace Lab*, Vol. 6, June 2014, pp. 1–15.
- [8] Howe, M., "On the Added Mass of a Perforated Shell, with Application to the Generation of Aerodynamic Sound by a Perforated Trailing Edge," *Proceedings of the Royal Society of London A*, Vol. 365, No. 1721, 1979, pp. 209–233. https://doi.org/10.1098/rspa.1979.0014
- [9] Khorrami, M. R., and Choudhari, M. M., "Application of Passive Porous Treatment to Slat Trailing Edge Noise," NASA TM-2003-2 1241, 2003.
- [10] Geyer, T. F., Sarradj, E., and Fritzsche, C., "Measurement of the Noise Generation at the Trailing Edge of Porous Airfoils," *Experiments in Fluids*, Vol. 48, No. 2, 2010, pp. 291–308. https://doi.org/10.1007/s00348-009-0739-x
- [11] Geyer, T. F., and Sarradj, E., "Trailing Edge Noise of Partially Porous Airfoils," 20th AIAA/CEAS Aeroacoustics Conference, AIAA Paper 2014-3093, 2014. https://doi.org/10.2514/6.2014-3039
- [12] Hajian, R., and Jaworski, J. W., "The Steady Aerodynamics of Aerofoils with Porosity Gradients," *Proceedings of the Royal Society A*, Vol. 473, No. 2205, 2017, Paper 20170266. https://doi.org/10.1098/rspa.2017.0266
- [13] Baddoo, P. J., Hajian, R., and Jaworski, J. W., "Unsteady Aerodynamics of Porous Aerofoils," *Journal of Fluid Mechanics*, Vol. 913, April 2021, Paper A16. https://doi.org/10.1017/jfm.2020.1031
- [14] Ayton, L. J., Colbrook, M. J., Geyer, T. F., Chaitanya, P., and Sarradj, E., "Reducing Aerofoil–Turbulence Interaction Noise Through Chordwise-Varying Porosity," *Journal of Fluid Mechanics*, Vol. 906, Jan. 2021,

- Paper A1.
- https://doi.org/10.1017/jfm.2020.746
- [15] Teruna, C., Manegar, F., Avallone, F., Ragni, D., Casalino, D., and Carolus, T., "Noise Reduction Mechanisms of an Open-Cell Metal-Foam Trailing Edge," *Journal of Fluid Mechanics*, Vol. 898, Sept. 2020, Paper A18. https://doi.org/10.1017/ifm.2020.363
- [16] Teruna, C., Avallone, F., Ragni, D., and Casalino, D., "On the Noise Reduction of a Porous Trailing Edge Applied to an Airfoil at Lifting Condition," *Physics of Fluids*, Vol. 33, No. 5, 2021, Paper 055132. https://doi.org/10.1063/5.0047512
- [17] Jiang, C., "Noise Generation by Airfoils and Rotors with Porous and Serrated Trailing Edges," Ph.D. Dissertation, Univ. of New South Wales, Australia, 2020. https://doi.org/10.26190/unsworks/2025
- [18] Chung, J., and Blaser, D., "Transfer Function Method of Measuring In-Duct Acoustic Properties. I. Theory," *Journal of the Acoustical Society of America*, Vol. 68, No. 3, 1980, pp. 907–913. https://doi.org/10.1121/1.384778
- [19] Chung, J., and Blaser, D., "Transfer Function Method of Measuring In-Duct Acoustic Properties. II. Experiment," *Journal of the Acoustical Society of America*, Vol. 68, No. 3, 1980, pp. 914–921. https://doi.org/10.1121/1.384779
- [20] Moreau, D. J., and Doolan, C. J., "Noise-Reduction Mechanism of a Flat-Plate Serrated Trailing Edge," *AIAA Journal*, Vol. 51, No. 10, 2013, pp. 2513–2522. https://doi.org/10.2514/1.J052436
- [21] Geyer, T. F., Sarradj, E., Giesler, J., and Hobracht, M., "Experimental Assessment of the Noise Generated at the Leading Edge of Porous Airfoils Using Microphone Array Techniques," 17th AIAA/CEAS Aeroacoustics Conference (32nd AIAA Aeroacoustics Conference), AIAA Paper 2011-2713, 2011. https://doi.org/10.2514/6.2011-2713
- [22] Jiang, C., Moreau, D., de Silva, C., and Doolan, C., "Noise Generation Mechanisms of a Micro-Tube Porous Trailing Edge," *Journal of Sound and Vibration*, Vol. 571, Feb. 2024, Paper 118085. https://doi.org/10.1016/j.jsv.2023.118085
- [23] Blake, W. K., Mechanics of Flow-Induced Sound and Vibration, Volume 2: Complex Flow-Structure Interactions, Academic Press, New York, 2017, pp. 424–426.
- [24] Vathylakis, A., Chong, T. P., and Joseph, P. F., "Poro-Serrated Trailing-Edge Devices for Airfoil Self-Noise Reduction," *AIAA Journal*, Vol. 53, No. 11, 2015, pp. 3379–3394. https://doi.org/10.2514/1.J053983
- [25] Koh, S. R., Meinke, M., and Schröder, W., "Numerical Analysis of the Impact of Permeability on Trailing-Edge Noise," *Journal of Sound and Vibration*, Vol. 421, May 2018, pp. 348–376. https://doi.org/10.1016/j.jsv.2018.02.017
- [26] Showkat Ali, S. A., Azarpeyvand, M., and da Silva, C. R. I., "Trailing Edge Bluntness Noise Reduction Using Porous Treatments," *Journal of Sound and Vibration*, Vol. 474, May 2020, Paper 115257. https://doi.org/10.1016/j.jsv.2020.115257
- [27] Liu, H., Hu, Z., Chen, N., Liu, Y., and Fan, H., "Structured Porous Blunt Trailing Edge with Uniform and Non-Uniform Parameters for Vortex Shedding Noise Reduction," *Applied Acoustics*, Vol. 206, April 2023, Paper 109302.
- https://doi.org/10.1016/j.apacoust.2023.109302
 [28] Bae, Y., Jeong, Y., and Moon, Y., "Effect of Porous Surface on the Flat Plate Self-Noise," 15th AIAA/CEAS Aeroacoustics Conference (30th AIAA Aeroacoustics Conference), AIAA Paper 2009-3311, 2009. https://doi.org/10.2514/6.2009-3311
- [29] Ffowcs Williams, J., and Hall, L., "Aerodynamic Sound Generation by Turbulent Flow in the Vicinity of a Scattering Half Plane," *Journal of Fluid Mechanics*, Vol. 40, No. 4, 1970, pp. 657–670. https://doi.org/10.1017/S0022112070000368
- [30] Kambe, T., Minota, T., and Ikushima, Y., "Acoustic Wave Emitted by a Vortex Ring Passing Near the Edge of a Half-Plane," *Journal of Fluid Mechanics*, Vol. 155, June 1985, pp. 77–103. https://doi.org/10.1017/S0022112085001720
- [31] Ffowcs Williams, J. E., "The Acoustics of Turbulence Near Sound-Absorbent Liners," *Journal of Fluid Mechanics*, Vol. 51, No. 4, 1972,

- pp. 737–749. https://doi.org/10.1017/S0022112072001338
- [32] Crighton, D. G., and Leppington, F. G., "Scattering of Aerodynamic Noise by a Semi-Infinite Compliant Plate," *Journal of Fluid Mechanics*, Vol. 43, No. 4, 1970, pp. 721–736. https://doi.org/10.1017/S0022112070002690
- [33] Yoas, Z., "Passive Trailing Edge Noise Attenuation with Porosity, Inspired by Owl Plumage," Ph.D. Dissertation, Pennsylvania State Univ., Univ. Park, PA, 2021.
- [34] Swann, M., Yoas, Z., Trzcinski, P., Nickels, A., and Krane, M., "Array Processing of Porous Trailing Edge Aeroacoustics," *Bulletin of the American Physical Society*, Vol. 67, 2022, https://meetings.aps.org/ Meeting/DFD22/Session/U11.5.
- [35] Sarradj, E., Fritzsche, C., Geyer, T. F., and Giesler, J., "Acoustic and Aerodynamic Design and Characterization of a Small-Scale Aeroacoustic Wind Tunnel," *Applied Acoustics*, Vol. 70, No. 8, 2009, pp. 1073–1080. https://doi.org/10.1016/j.apacoust.2009.02.009
- [36] Geyer, T. F., and Enghardt, L., "Noise Generation by Two Staggered Circular Cylinders of Equal Diameter in Cross-Flow," 28th AIAA/CEAS Aeroacoustics Conference, AIAA Paper 2022-3093, 2022. https://doi.org/10.2514/6.2022-3093
- [37] Sarradj, E., and Herold, G., "A Python Framework for Microphone Array Data Processing," *Applied Acoustics*, Vol. 116, Jan. 2017, pp. 50–58. https://doi.org/10.1016/j.apacoust.2016.09.015
- [38] Welch, P., "The Use of Fast Fourier Transform for the Estimation of Power Spectra: A Method Based on Time Averaging over Short, Modified Periodograms," *IEEE Transactions on Audio and Electroacoustics*, Vol. 15, No. 2, 1967, pp. 70–73. https://doi.org/10.1109/TAU.1967.1161901
- [39] Sijtsma, P., "CLEAN Based on Spatial Source Coherence," *International Journal of Aeroacoustics*, Vol. 6, No. 4, 2007, pp. 357–374. https://doi.org/10.1260/147547207783359459
- [40] Dougherty, R. P., "Functional Beamforming," 5th Berlin Beamforming Conference, Soc. for the Advancement of Applied Computer Science, 2014, pp. 19–20.
- [41] Glegg, S., and Devenport, W., "Aeroacoustics of Low Mach Number Flows: Fundamentals, Analysis, and Measurement," Academic Press, 2017, pp. 593–622.
- [42] White, F. M., and Majdalani, J., Viscous Fluid Flow, Vol. 3, 4th ed., McGraw-Hill, New York, 2021, pp. 274–276.
- [43] Brooks, T. F., Pope, D. S., and Marcolini, M. A., "Airfoil Self-Noise and Prediction," NASA RP-1218, NASA Langley Research Center, 1989.
- [44] Ananthan, V. B., Akkermans, R. A., Hu, T., Liu, P. Q., and Rathje, N., "Trailing-Edge Noise Reduction Potential of a Locally Applied Shallow Dimpled Surface," *Journal of Sound and Vibration*, Vol. 525, May 2022, Paper 116745. https://doi.org/10.1016/j.jsv.2022.116745
- [45] Herold, G., and Sarradj, E., "Performance Analysis of Microphone Array Methods," *Journal of Sound and Vibration*, Vol. 401, Elsevier, Aug. 2017, pp. 152–168. https://doi.org/10.1016/j.jsv.2017.04.030
- [46] McTavish, S., Feszty, D., and Nitzsche, F., "Evaluating Reynolds Number Effects in Small-Scale Wind Turbine Experiments," *Journal of Wind Engineering and Industrial Aerodynamics*, Vol. 120, Sept. 2013, pp. 81–90. https://doi.org/10.1016/j.jweia.2013.07.006
- [47] Gennaro, E. M., Colaciti, A. K., and Medeiros, M. A., "On the Controversy Regarding the Effect of Flow Shear on the Strouhal Number of Cylinder Vortex Shedding," *Aerospace Science and Technology*, Vol. 29, No. 1, 2013, pp. 313–320. https://doi.org/10.1016/j.ast.2013.04.002
- [48] Feng, Z., and Ye, Q., "Turbulent Boundary Layer over Porous Media with Wall-Normal Permeability," *Physics of Fluids*, Vol. 35, No. 9, 2023, Paper 095111. https://doi.org/10.1063/5.0160773

X. Zhang Associate Editor